Highly tunable magnetocrystalline anisotropy energy in Fe^{3+}-doped $BaTiO_3$

Bradford A. Barker[1,2],* Nabaraj Pokhrel[3], Md Kamal Hossain[3],
Katherine Inzani[4], Sinéad M. Griffin[5,6], and Elizabeth A. Nowadnick[1]
[1] *Department of Chemical and Materials Engineering, University of California, Merced, CA 95340, USA*
[2] *Department of Engineering Physics, Florida Polytechnic University, Lakeland, FL 33805, USA*
[3] *Department of Physics, University of California, Merced, CA 95340, USA*
[4] *School of Chemistry, University of Nottingham, Nottingham NG7 2RD, United Kingdom*
[5] *Materials Sciences Division, Lawrence Berkeley National Laboratory, Berkeley, California 94720, USA and*
[6] *Molecular Foundry, Lawrence Berkeley National Laboratory, Berkeley, California 94720, USA*

Magnetic dopants in ferroelectric oxide host materials provide a platform for electric field control of isolated spins, facilitated by tuning of the magnetocrystalline anisotropy energy (MCAE). We present first-principles calculations of the MCAE experienced by isolated Fe^{3+} dopants in the tetragonal, orthorhombic, and rhombohedral phases of the prototypical ferroelectric $BaTiO_3$. We identify an order-of-magnitude decrease in the MCAE in the rhombohedral phase, relative to the tetragonal and orthorhombic phases. We explain this dramatic decrease, as well as the formation of a spin-easy plane in the tetragonal phase and spin-easy axes in the orthorhombic and rhombohedral phases, using crystal field theory arguments. Building a superposition model from crystal field theory, we show how a set of simple criteria based on crystalline environment can be used to estimate the MCAE. We suggest this as a route to rapidly screen candidate ferroelectric hosts and magnetic dopants that possess phases with spin easy axes and maximal MCAE tunability.

I. INTRODUCTION

Controlling the spin degree of freedom with electric fields in materials is appealing for its potential in spintronics[1, 2] and quantum information processing [2–4]. The electric-field control over spin offers several advantages to magnetic-field control: they typically require less energy for switching, and they enable control over smaller length- and time-scales [5, 6]. This has driven substantial research into the fundamental physics of magnetoelectric coupling mechanisms as well as materials that exhibit and enhance this property. Examples of electric control of spin properties include the electric field modulation of spin-spin interactions [7] and spin transitions[8], and the field of magnetoelectric multiferroics [9–11]. Recent studies have pushed towards the atomic-scale limit, considering electric field control of molecular and even single-atom magnets [12–15] with the ultimate goal of electric field-based single spin processing for both classical and quantum computing.

Complementing molecular magnets where design of ligand fields provide exceptional tunability over spin functionality [16], oxides with dilute magnetic dopants provide offer highly tunable crystal-field environments. In particular, if these are ferroelectric oxides, electric-field-induced structural changes can result in the modification of the magnetocrystalline anisotropy energy (MCAE), enabled by magnetoelectric coupling. A combination of the magnetic ion's spin-orbit coupling strength together with its local crystalline environment provided by the ferroelectric host determines its MCAE. This gives the magnetic dopant spin an energetic preference for certain orientations with respect to the lattice, which in principle can be modified by local crystal field changes induced by electric field-based polarization switching in the ferroelectric host. Recent investigations of Fe^{3+} dopants in ferroelectric $PbTiO_3$ and Bi_2WO_6 hosts demonstrated the feasibility of this approach by showing that 90° flips in the ferroelectric polarization direction can control the orientation of spin-easy planes and axes, respectively [17, 18].

Due to their rich chemical and structural diversity, ferroelectric oxide hosts hold great potential for designing MCAEs to enable electric field control of spin directionality. Tunable MCAEs are particularly desirable, whereby large MCAE values can enable information storage with stable spin directionality, followed by lowering of the MCAE to manipulate to spin direction with minimal energetic cost. However, there is still limited understanding of how modulations to the local crystalline symmetry environment of a single magnetic ion translates into its MCAE.

Here, we address this problem using first-principles calculations on the model system of Fe^{3+}-doped ferroelectric $BaTiO_3$. $BaTiO_3$ is an ideal ferroelectric host for this study because it has three distinct ferroelectric phases, thus any changes to the MCAE of a magnetic dopant as the material traverses these phases can be tied directly to the changes in crystalline environment. At room temperature, bulk $BaTiO_3$ crystallizes in a tetragonal (T) phase with $P4mm$

* bbarker@floridapoly.edu

symmetry (space group #99), and as temperature lowers it transitions to an orthorhombic (O) $Amm2$ phase (s.g. #38) at 278 K, followed by a rhombohedral (R) $R3m$ phase (s.g. #160) at 183 K [19, 20]. The polarization arises from an off-centering of the Ti^{4+} cation with respect to the oxygen sublattice due to the second-order Jahn-Teller effect [21]. As shown in Figure 1(a-c), the polarization in the tetragonal, orthorhombic, and rhombohedral phases lies along ⟨001⟩, ⟨110⟩, and ⟨111⟩, respectively. In thin films, these three ferroelectric phases are also accessible via epitaxial strain [22].

Previous Electron Paramagnetic Resonance (EPR) studies of Fe^{3+} dopants in $BaTiO_3$ showed a spin-easy plane in the T phase oriented perpendicular to its ferroelectric polarization, a spin-easy axis in the O phase along ⟨001⟩ perpendicular to its ferroelectric polarization along ⟨110⟩, and a spin-easy axis in the R phase parallel to its ferroelectric polarization along ⟨111⟩ [23–25]. The magnitude of the MCAE decreases as $BaTiO_3$ traverses between these phases, with the MCAE in the R phase being an order of magnitude smaller than it is in the other two phases. This drastic reduction of the MCAE in the R phase is surprising because all three phases have roughly the same polarization and Ti displacement. Subsequent theoretical work explained this phenomenon using the semi-empirical Superposition Model method [26, 27], assuming a significant reduction in the ferroelectric displacement of the Fe^{3+} ion, compared to that of Ti^{4+} [28]. Such a reduction of the ferroelectric distortion at the magnetic dopant site is plausible, because the partially filled d orbitals of the dopant (in the case of Fe^{3+}, half-filled) reduce the magnitude of the second-order Jahn-Teller effect [21]. This contrasts with previous work on Gd^{3+}-doped $BaTiO_3$, which showed little variation in its MCAE between the T, O, and R phases [28, 29], which can be understood because the unfilled d shells in lanthanides allow for the retention of the ferroelectric distortion. These results suggest that transition metal dopants, despite exhibiting lower spin-orbit coupling strengths compared to lanthanides, provide a promising pathway to highly controllable MCAEs.

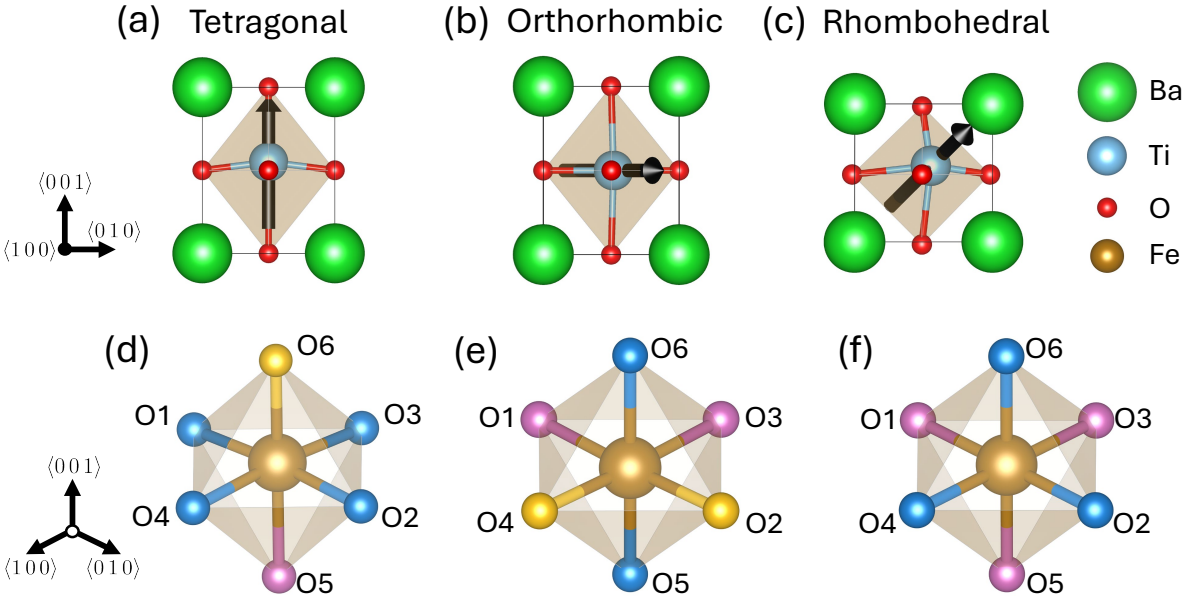

FIG. 1. (a-c) Primitive unit cells and polarization vector for (a) tetragonal $P4mm$, (b) orthorhombic $Amm2$, (c) rhombohedral $R3m$ $BaTiO_3$. (d-f) Local octahedral environment about the Fe^{3+} dopant, with symmetry-equivalent oxygens denoted by oxygen coloration: (d) tetragonal $P4mm$, (e) orthorhombic $Amm2$, (f) rhombohedral $R3m$. The shortest bond lengths are coded with yellow O atoms, intermediate with blue, and longest with purple.

II. COMPUTATIONAL METHODS

We use Density Functional Theory (DFT) to calculate the MCAE surfaces Fe^{3+} in $BaTiO_3$, using supercells to model a dilute concentration. We employ the PBEsol [30] exchange-correlation functional in a plane-wave basis with the Vienna Ab initio Simulation Package [31–35]. We substitute Fe^{3+} for Ti^{4+}, adding one electron for charge compensation, and include a Hubbard U correction of 4.0 eV on the $3d$ orbitals of Fe within the Dudarev scheme [36].

This U choice is within the range of appropriate U values for Fe obtained by linear response calculations on a database of transition metal oxides [37]. It also is consistent with prior work on Fe^{3+} dopants in similar systems[17]. Fe^{3+} substitutions for Ti^{4+} in ABO_3 perovskites [23, 38] can also be accompanied by an oxygen vacancy to give a defect complex with an overall neutral charge. DFT+U calculations in Ref. [17] indicate the Fe^{3+}-V_O complex has qualitatively similar MCAE surfaces to the individual substitutional defect studied here.

We employ a 600 eV plane-wave basis cutoff, which converges total energies for the T phase to within 10 meV/f.u. compared to an 800 eV cutoff. Structural relaxations of undoped $BaTiO_3$ are performed in a 5-atom primitive cell with a Γ-centered 6×6×6 k-point grid, which gives relaxed lattice parameters within 0.001 Å of those computed with an 8×8×8 k-point grid. Agreement with experiment[39, 40] for the lattice parameters is within 1%. Doping calculations are performed by replacing one Ti atom with a Fe atom in a 3×3×3 supercell of $BaTiO_3$ (135 atoms). Calculations in the supercells employ a Γ point-centered 2×2×2 k-grid. Induced magnetic moments are not observed on any of the non-Fe ions in the supercell.

We employ VASP pseudopotentials with Fe $3p\,3d\,4s$ (Fe_pv), Ba $5p\,6s$ (Ba_sv), Ti $3p\,3d\,4s$ (Ti_pv), O $2s\,2p$ (O), K $3s\,3p\,4s$ (K_sv), Nb $4s\,4p\,5s\,4d$ (Nb_sv), and Pb $6s\,5d\,5p$ (Pb_d) states treated as valence. Total energies are converged to 10^{-6} eV within the self-consistent field (SCF) loop, and forces are converged to 1 meV/Å and 10 meV/Å during structural relaxation for the undoped primitive cells and doped supercells, respectively. The volume of the supercell is held fixed during structural relaxation. SCF total energies for the non-collinear calculations are converged to 10^{-7} eV.

The DOS calculations are performed without spin-orbit coupling, using a k-grid sampling of 3×3×3. The supercell axes for these calculations are chosen such that the c axis coincides with the z axis, and the a and b axes are oriented as closely as possible to the x and y axes, respectively.

The MCAE is computed from the total energies from non-collinear SCF calculations that incorporate spin-orbit coupling, with a Γ point-centered k-grid sampling of 2×2×2. The spin axes are oriented on 194 points on the unit sphere from 23rd order Lebedev quadrature [41, 42], by PyMatGen using available symmetries as found from the `spglib` library [43, 44].

The FINDSYM software [45] from the ISOTROPY Software Suite is used for group theoretic analysis and VESTA [46] is used for crystal structure visualization.

III. RESULTS

A. Magnetocrystalline anisotropy energy

Figure 2 presents our DFT-computed MCAE surfaces for the T, O, and R phases of $BaTiO_3$. The MCAE of each phase is given by the energy difference between maximum and minimum values on the MCAE surface. For the T phase, the MCAE is 82 μeV with a spin-easy plane, consistent with previous calculations of Fe^{3+}-doped $PbTiO_3$ [17]. In the O phase, the MCAE reduces to 33 μeV with a spin-easy axis along [001], and in the R phase the MCAE is further reduced to 4 μeV with a spin-easy axis along [111]. We fit the MCAE surfaces in Fig. 2 to functions suitable to each crystal symmetry in order to obtain the magnetic anisotropy constants K for each phase (given in Appendix A).

To compare our computed MCAEs to experimental values, we recast them in a form accessible from the zero-field spin Hamiltonian [27], used to extract magnetic anisotropies from experimental EPR spectra:

$$H_S = \sum_{k,q} b_k^q \, f_k \, \hat{O}_k^q(\mathbf{S}) \,, \tag{1}$$

where k and q are the major and minor ranks, respectively, for the tensorial Stevens operators $\hat{O}_k^q(\mathbf{S})$ with coefficients b_k^q (see Ref. [27] for a compilation of the Stevens operators through rank $k = 6$). f_k is a numerical factor, with $f_2 = 1/3$. Magnetic anisotropy energies, to leading order, come from the $k = 2$, $q = 0$ term in Eq. 1 [27]:

$$H_S^{aniso} \approx \frac{1}{2} b_2^0 \, (S_z^2 - \frac{1}{3} S(S+1)) \,. \tag{2}$$

Obtaining the MCAE within this framework requires calculating the energy difference between evaluating Eq. 2 with the spin oriented along the $\langle 0\,0\,1 \rangle$ axis ($\perp$, by convention) and along the $\langle 1\,0\,0 \rangle$ axis ($\parallel$). For a $S = 5/2$ ion such as

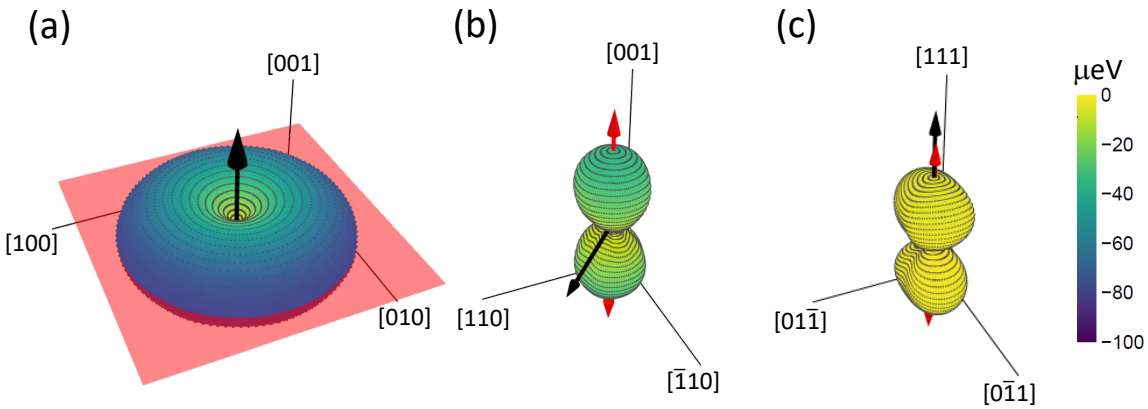

FIG. 2. MCAE surfaces for the (a) tetragonal, (b) orthorhombic, and (c) rhombohedral phases of $BaTiO_3$. The spin-easy plane in (a) is denoted by a red plane, and the spin-easy axes in (b,c) are denoted by red arrows. Polarization vectors are denoted by black arrows. The coordinate axes refer to lattice vectors particular to each phase of $BaTiO_3$

Fe^{3+}, this requires evaluating the matrix elements (with the assistance of tables from Ref. [47]):

$$\begin{aligned} & E_\perp - E_\parallel \\ & = \langle S = 5/2,\, \perp \,|\, b_2^0\, f_2\, \hat{O}_2^0(\mathbf{S}) \,|\, S = 5/2,\, \perp \rangle \\ & \quad - \langle S = 5/2,\, \parallel \,|\, b_2^0\, f_2\, \hat{O}_2^0(\mathbf{S}) \,|\, S = 5/2,\, \parallel \rangle \\ & = 5\, b_2^0\,. \end{aligned} \tag{3}$$

The key result here is that to lowest order in the spin Hamiltonian, the MCAE is 5 times the anisotropy constant b_2^0 (b_2^0 is often reported as D in literature). Full details of the derivation are provided in the SI [48] (see also references [49–54]).

Table I compares the spin Hamiltonian parameter b_2^0 obtained from our DFT+U calculations for each of the three phases of $BaTiO_3$ with experimental values taken from Ref. [55]. We observe good agreement between the computed and experimental values, with DFT providing a slight overestimate for the T and R phases. In both DFT and experiment, b_2^0 is positive in the T phase and negative in the O and R phases, indicating a spin-easy plane and spin-easy axis, respectively. This level of agreement between theory and experiment is particularly impressive given the small energy scale of the MCAE.

TABLE I. Spin Hamiltonian parameter b_2^0 calculated with DFT+U in the present work and reported experimental values for the tetragonal [23–25, 56–61], orthorhombic [24], and rhombohedral [25, 62] phases.

b_2^0 (10^{-4} cm^{-1})	Tetragonal	Orthorhombic	Rhombohedral
DFT+U	1315	-608	-36
Experiment	890 – 991	-530 – -640	-19 , -23

TABLE II. Comparison of the B-site transition metal displacement Δ away from the central position in the octahedron for the three phases of $BaTiO_3$. Δ^{Ti} is computed for an undoped primitive unit cell, and Δ^{Fe} is computed in the Fe-doped supercell. Values of Δ for all Ti^{4+} ions in the supercells are presented in the SI [48].

phase	Δ^{Ti} (Å)	Δ^{Fe} (Å)	$\Delta^{\mathrm{Fe}} - \Delta^{\mathrm{Ti}}$ (Å)
Tetragonal	0.400	0.368	-0.032
Orthorhombic	0.098	0.034	-0.064
Rhombohedral	0.084	0.003	-0.081

B. Origin of MCAE reduction

We next seek to understand the origin of the large reduction in MCAE upon going between the three phases of $BaTiO_3$. Figure 1(d-f) indicates the symmetry of the local crystalline environment about the Fe^{3+} dopant in each of these three phases, with symmetry-equivalent oxygen atoms denoted by the same color. The atoms that lie in planes perpendicular to the polar displacement form one symmetry-equivalent set (e.g. the equatorial oxygens O1-O4 in the T phase and the apical oxygens O5 and O6 in the O phase in Fig. 1). The oxygens which the Ti displaces towards and away from are symmetry-distinct. The T and O phases have three symmetry-distinct oxygen positions, whereas the R phase has just two. The symmetries of the pristine crystal are preserved for the defected supercells, so the point groups at the Fe^{3+} defect site are C_{4v}, C_{2v}, and C_{3v} for the T, O, and R phases, respectively.

One approach to arrive at the MCAE values for these three phases of different symmetry is to use conventional perturbation theory to evaluate corrections to the total energy of the (spin-collinear) supercells upon inclusion of spin-orbit coupling matrix[52, 63]. Such an approach involves the evaluation of matrix elements between occupied and unoccupied Fe d states, so that the projected density of states (pDOS) can be used to quickly estimate the MCAE. Figure 3 shows the DOS and pDOS for the T, O, and R phases of $BaTiO_3$, with the e_g and t_{2g} states highlighted in green and blue, respectively. We find that the e_g and t_{2g} states are qualitatively very similar in the three phases, indicating that the the cubic electrostatic field of the oxygen ligands about the Fe^{3+} defect is similar in all the phases, despite the changes to the local crystalline environment discussed above (this also is consistent with experiment[55]). We thus seek an alternative approach for understanding the order of magnitude reduction of the MCAE value, as well as the influence of the symmetry of the crystalline environment in determining a spin-easy axis or plane. Although approaches based on treating the axial crystalline electrostatic potential as a perturbation to the cubic field provide physical insight[64], we instead prefer a direct approach, evaluating the axial coefficients of the spin Hamiltonian using methods developed in Crystal Field Theory, including the Superposition Model[26].

As noted in Sec. I, Ref. [28] successfully explained experimental trends in the sign and magnitude of b_2^0 (and hence the MCAE) in Fe^{3+}-doped $BaTiO_3$ using a Superposition Model analysis with a "centered" Fe^{3+} dopant with no polar displacement (and no oxygen displacements). Motivated by this result, we computed the displacement Δ of the Ti and Fe ions away from the octahedral center position using our DFT+U-optimized supercells for the three phases of $BaTiO_3$. Table II shows that our computed Δ for Fe^{3+} is less than that for Ti^{4+} in all three phases. Compared to the Ti^{4+} displacements, the Fe^{3+} ion loses 0.03 Å, 0.06 Å, and 0.08 Å of displacement, which corresponds to a 8%, 65% and 96% reduction, in the T, O, and R phases, respectively. Strikingly, the Fe^{3+} ion in the R phase returns very nearly to the center of the octahedron. The larger center-seeking displacements in the O and R phases are consistent with the diminished MCAE in these phases, compared to the T phase [28]. To our knowledge, experimental values for these local Fe displacements are not available, so our first-principles results provide confirmation of Ref. [28]'s proposed explanation linking the significant differences in b_2^0 values in the three phases of Fe^{3+}-doped $BaTiO_3$ to the centering of the magnetic ion.

Our computational confirmation of the Fe^{3+} dopant-centering behavior suggests that we may be able to analytically determine trends in MCAE values for different combinations of ferroelectric hosts and magnetic dopants using a Superposition Model analysis analogous to that performed in Ref. [28]. Compared to computationally expensive DFT+U MCAE surface calculations, the Superposition Model approach only requires experimental (or DFT-calculated) lattice parameters and ionic coordinates as input. The Superposition Model [26, 27] is a phenomenological approach which yields physical insight, although perturbative approaches for calculating b_2^0 for ^6S magnetic ion dopants also have been determined [64–66]. This model assumes that the contribution to b_2^0 from each ligand may be considered independently with each initially oriented along the quantization axis, and then finally the metal ion–ligand bonds are rotated to constitute the actual polyhedron. The Superposition Model was initially developed for crystal electric fields, where vector rotations are appropriate. With $L = 0$ for a ^6S magnetic ion such as Fe^{3+}, the tensor product of the spin operator with the ground state transforms as a vector, and the Superposition Model also applies for the spin Hamiltonian [27]. The Superposition Model's assumption that the crystal field at a magnetic ion is a superposition of the contributions from each ligand is strictly true if the interactions are between electrostatic point charges. In the presence of quantum mechanical effects such as overlap between the magnetic ion orbitals and those of its neighboring ligands, this assumption remains valid in the limit of small inter-ligand charge penetration. This is a reasonable assumption because the stronger electrostatic repulsion between the ligands prevents an appreciable contribution from the inter-ligand charge penetration. An additional assumption of the Superposition Model is that only nearest-neighbor ligands make a contribution, since further neighbors have minimal orbital overlap with the magnetic ion [27].

Figure 4 summarizes the key features of the Superposition Model relevant for our analysis. To obtain b_2^0 values from crystal structure parameters, the Superposition Model requires a scaling of the single-ligand parameter with respect to distance. A common choice is to assume a simple power-law scaling with respect to the transition metal ion–ligand bond length R_i:

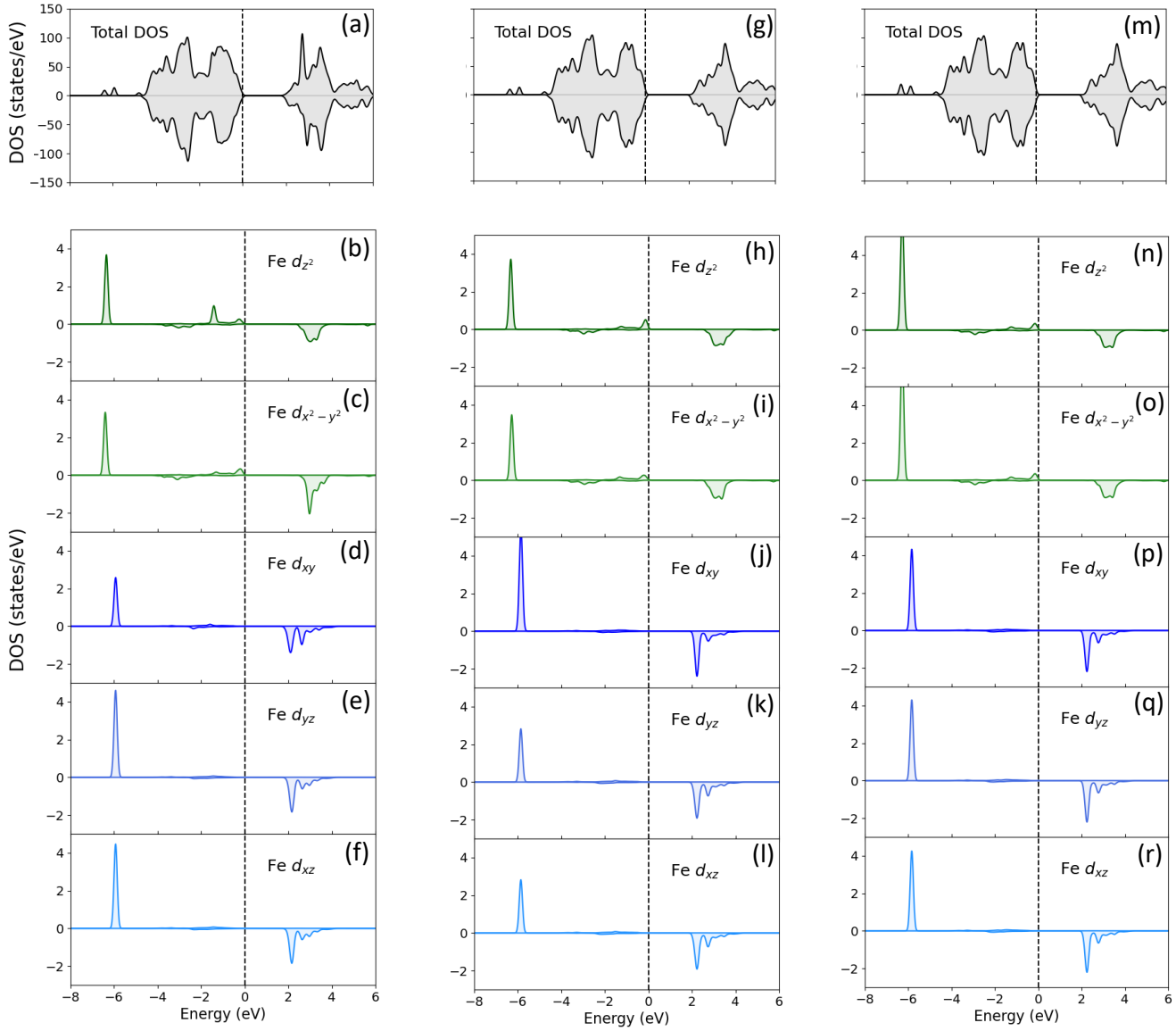

FIG. 3. Total and projected density of states. Tetragonal $P4mm$: (a-f). Orthorhombic $Amm2$: (g-l). Rhombohedral $R3m$: (m-r). Total density of states: a, g, and m. Fe atomic orbital resolved projected density of states with e_g states in green and t_{2g} states in blue.

$$b_2^0 = \sum_{i \in \text{Ligands}} \bar{b}_2(R_0) \left(\frac{R_0}{R_i}\right)^{t_2} \frac{1}{2}(3\cos^2\theta_i - 1)\,. \tag{4}$$

Here $\bar{b}_2$ is an intrinsic parameter that depends primarily on the species, charge, and spin-orbit coupling strength of the transition metal ion and its ligand, R_0 is a typical ion–ligand distance at which $\bar{b}_2$ is evaluated (Fig. 4(a)), t_2 is the power law constant, and the last term is the $k = 2$, $q = 0$ form factor that accounts for the angle θ_i between the transition metal–ligand bond R_i and the z axis (Fig. 4(b)) [67].

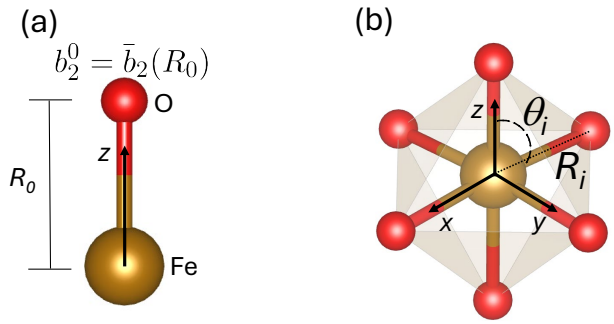

FIG. 4. Key components of the Superposition Model. (a) The magnetic ion–ligand bond, with length R_0, is taken to be along the z axis. The coefficient b_2^0 for the spin Hamiltonian from this isolated ion–ligand bond defines the intrinsic parameter $\bar{b}_2(R_0)$. (b) Now considering multiple ligands, each ion–ligand bond gives a contribution to b_2^0 determined by the particular bond length R_i (dashed line) and polar angle θ_i (dashed-dotted line). The z-axis must be chosen to coincide with the axis of maximal symmetry [67].

For an Fe^{3+} ion with O ligands, Ref. [28]'s Superposition Model analysis fit experimental data to obtain $\bar{b}_2(R_0) = -0.412$ cm^{-1} with $R_0 = 2.101$ Å [68] and $t_2 = 8$. Using our DFT+U-computed b_2^0 from Table I together with DFT-relaxed R_i values for the T phase, and assuming the same values of R_0 and t_2 as given above, we solve Eq. 4 to obtain a first principles-based $\bar{b}_2(R_0) = -0.437$ cm^{-1}, in good agreement with the value fitted from experiment.

In a centered model, where the transition metal ion is not displaced from its high-symmetry position at the center of the transition metal-oxygen octahedron, Eq. 4 reduces to the following analytic expressions [28]

$$b_2^0(T) = 2\bar{b}_2(R_0)\left(\frac{R_0}{c/2}\right)^{t_2}\left(1-(c/a)^{t_2}\right) \tag{5}$$

$$b_2^0(O) = 2\bar{b}_2(R_0)\left(\frac{R_0}{a/2}\right)^{t_2}\left(1-\left(\frac{2a}{\sqrt{b^2+c^2}}\right)^{t_2}\right) \tag{6}$$

$$b_2^0(R) = 6\bar{b}_2(R_0)\left(\frac{R_0}{a/2}\right)^{t_2}\left(2\cos^2(\alpha/2)-1\right) \tag{7}$$

for the T, O, and R phases, respectively. Here a, b, and c are the lattice parameters appropriate for each phase (with the convention that the c axis is the polarization direction in the T and O phases), and α is the rhombohedral angle.

Equations 5-7 provide insight into the MCAE evolution in the three phases of $BaTiO_3$. From Eq. 7 we can explain the small MCAE in the R phase because the rhombohedral angle α is a small deviation $\epsilon \approx 0.13°$ from $\pi/2$ (that is, $\alpha = \pi/2 - \epsilon$) for $BaTiO_3$. Rewriting the angular factor in Eq. 7 as $(2\cos^2(\alpha/2) - 1) = \sin\epsilon$, it is immediately clear for small ϵ, this term is proportional to ϵ and hence $b_2^0(R) \propto \epsilon$. In addition, the strain-polarization coupling in ferroelectrics will always yield $(c/a) > 1$ in the T phase and $2a/\sqrt{b^2+c^2} < 1$ in the O phase, which imply a spin-easy plane and axis, respectively. These expressions also make clear how changing the lattice parameters can tune the MCAE value, for example to create large MCAEs in the T phase one should target ferroelectric hosts with large c/a ratios.

Table III presents centered model estimates of b_2^0 for the three phases of $BaTiO_3$, computed from Eqs. 5-7 using experimental lattice constants for the T and O phases from Ref. [69] and for the R phase from Ref. [40], and our first principles-based $\bar{b}_2$ value given above. The centered model reproduces the sign of b_2^0 for all three phases. The b_2^0 magnitudes are quite close to the experimental values, and the reduction in magnitude going from the T to R phase is captured. We note that the level of agreement between the centered model and first-principles b_2^0 values for the T phase is striking, given that the Fe ion retains a significant ferroelectric displacement in this phase (Table II). This can be understood as arising from a fortuitous cancellation of errors in the centered model for the T phase, because both the Fe offcentering as well as the accompanying oxygen displacements are neglected (see the SI for further discussion).

We also construct centered-model b_2^0 estimates using DFT-computed lattice parameters (see Appendix B), and find that they also reproduce the MCAE trends. However, care must be taken because the t_2 exponential in Eqs. 5-7 makes the results highly sensitive to small changes in lattice parameter values, and therefore dependent on the choice of

TABLE III. Estimates of b_2^0 (in 10^{-4} cm^{-1}) from the centered model for specified magnetic dopants in specified hosts. For Fe^{3+} dopants we use our first principles-computed $\bar{b}_2(R_0)$=-0.437 cm^{-1} and t_2=8, and for Mn^{2+} dopants we use $\bar{b}_2(R_0)$=-0.1575 cm^{-1} and t_2=7, taken from Ref. [28].

Ion	Host	Geometry	Centered model	Experiment
Fe^{3+}	$BaTiO_3$ (T)	$a = 3.986$ Å, $c/a = 1.01$ [69]	1023	890 – 991 [23–25, 56–61]
Fe^{3+}	$BaTiO_3$ (O)	$a = 3.990$ Å, $b = 5.669$ Å, $c = 5.682$ Å [69]	-599	-530 – -640 [24]
Fe^{3+}	$BaTiO_3$ (R)	$a = 4.004$ Å, $\alpha = 89.87°$ [40]	-88	-19, -23 [25, 62]
Fe^{3+}	$KNbO_3$ (T)	$a = 3.996$ Å, $c/a = 1.017$ [70]	1628	
Fe^{3+}	$KNbO_3$ (O)	$a = 3.971$ Å, $b = 5.692$ Å, $c = 5.719$ Å [70]	-1635	-1776 [71]
Fe^{3+}	$KNbO_3$ (R)	$a = 4.016$ Å, $\alpha = 89.817°$ [70]	-120	
Mn^{2+}	$BaTiO_3$ (T)	$a = 3.986$ Å, $c/a = 1.01$ [69]	307	215 [72]
Mn^{2+}	$BaTiO_3$ (O)	$a = 3.990$ Å, $b = 5.669$ Å, $c = 5.682$ Å [69]	-180	
Mn^{2+}	$BaTiO_3$ (R)	$a = 4.004$ Å, $\alpha = 89.87°$ [40]	-29	
Fe^{3+}	$PbTiO_3$ (T)	$a = 3.905$ Å, $c/a = 1.063$ [73]	6070	5300 [74]

exchange-correlation functional. Taking the example of tetragonal $BaTiO_3$, the lattice parameters calculated with the PBEsol functional are are $a = 3.970$ Å, $c/a = 1.020$, yielding b_2^0=2019×10^{-4}cm^{-1} which is a significant overestimate. In contrast, the LDA lattice parameters are $a = 3.943$ Å, $c/a = 1.013$, yielding b_2^0=1384×10^{-4}cm^{-1} which is in better agreement with the experimental value in Table III. In summary, these results show that the b_2^0 spin Hamiltonian coefficients, and therefore the magnitude and sign of the MCAE for each phase can in principle be reconstituted from a small set of parameters and the geometric information of the oxygen ligands.

C. Extension to other ferroelectric hosts and magnetic dopants

We next test whether the Superposition Model with a centered magnetic dopant can explain MCAE trends in other ferroelectric host materials. As a first test case, we consider an Fe^{3+} dopant in $KNbO_3$, which exhibits the same sequence of three ferroelectric structures as $BaTiO_3$ [75]. Table III shows our estimated b_2^0 values, obtained with experimental lattice parameters from Ref. [70] (see the SI for analogous results using DFT lattice parameters). We observe good agreement between the centered model estimate of the O-phase MCAE and the experimental value (Table III). Like $BaTiO_3$, the T phase displays a spin-easy plane (positive b_2^0) whereas the O and R phases display spin easy axes (negative b_2^0), and there is an order-of-magnitude diminution of the MCAE going from the O to the R phase. As a second test case, we consider a Fe^{3+} dopant in tetragonal $PbTiO_3$ (Table III). The MCAE is significantly larger than in tetragonal $BaTiO_3$ and the centered model prediction shows reasonable agreement with experiment. This increased MCAE can be attributed to the larger c/a ratio in $PbTiO_3$ compared to $BaTiO_3$.

The level of agreement between the experimental and centered-model MCAEs in Table III for Fe-doped $KNbO_3$ and $PbTiO_3$ is quite remarkable, given that the centered model does not explicitly depend on the spin-orbit coupling strength λ_{SOC} of the ferroelectric host material: changing the host just modifies the lattice parameters in Eqs. 5-7. Compared to $BaTiO_3$, Nb^{5+} has a larger spin-orbit coupling than Ti^{4+}, and Pb^{2+} has a significantly larger spin-orbit coupling than Ba^{2+}. Although the host's spin-orbit coupling does implicitly help determine the experimental lattice parameters, one would naively expect that the lack of explicit λ_{SOC} dependence in the centered model would yield b_2^0 estimates that are significantly lower than the experimental values. This is not the case, however, demonstrating the unexpectedly large impact of the local crystal field environment of the host in determining MCAE surfaces.

As a final test case, we consider Mn^{2+} dopants in the three phases of $BaTiO_3$. The intrinsic parameter $\bar{b}_2$ for Mn^{2+} is roughly one-third that of Fe^{3+} for oxygen ligands at the same distance [68] due to the reduction of the spin-orbit coupling strength[76], so we may expect a reduction in the MCAE by a similar factor. Using the Superposition Model parameters $\bar{b}_2$, R_0, and t_2 from Ref. [68], our centered-model estimates for b_2^0 with Mn^{2+} are indeed roughly one-third of those of Fe^{3+}, for all three phases (Table III). The experimentally determined MCAE value for a Mn^{2+} dopant in tetragonal $BaTiO_3$ is nearly five times smaller than Fe^{3+} (see Table III). This may be because the centered model estimates do not take into account the dopant ionic size: Ti^{4+} and Fe^{3+} have similar ionic radii, whereas Mn^{2+} is larger, which would lead to an expansion of the lattice parameters.

IV. DISCUSSION

Finally, we use our results to formulate criteria for selecting combinations of magnetic dopants and ferroelectric hosts that exhibit large MCAE magnitudes together with high tunability. The small (<100 μeV) MCAE energy scale

for Fe^{3+} dopants in $BaTiO_3$ would require very low temperature operation (≈1 K) in order to avoid thermally-induced spin switching. This is above the typically mK operating temperature of some quantum devices, however, in general higher temperature operation is desirable for applications. In addition, larger MCAEs would be easier to disentangle from other physical processes in materials that occur at low energy scales. Although lanthanide ions provide large spin-orbit coupling strengths, they retain the ferroelectric displacements of their hosts and therefore do not provide tunable MCAEs [28, 29], thus leading us to focus on transition metal dopants with partially filled d shells. Fe^{3+} and Mn^{2+} are both $L = 0$ dopants which have large effective magnetic moments due to their half-filled d-shells. However, they have fairly small spin-orbit coupling strengths [76] ($H_{\mathrm{SOC}} = \lambda_{\mathrm{SOC}}\,\mathbf{L}\cdot\mathbf{S}$), which limits the magnitude of their MCAE values. Transition metal dopants with $L \neq 0$ as free ions may exhibit a larger magnitude MCAE, for example, a neutral Co adatom has been reported to exhibit the atomic limit of magnetic anisotropy energy [77]. Transition metal ion candidates with relatively large effective magnetic moments [78], non-zero L as free ions, ionic radii close to that of Ti^{4+}, and a spin-orbit coupling larger than Fe^{3+} [76] include Ni^{3+}, Co^{3+}, and Co^{2+} (see the SI for more details [48]). We note that the Superposition Model no longer formally applies for the $L \neq 0$ ions, so first-principles calculations are needed to assess the MCAEs of these dopants.

In selecting ABO_3 ferroelectric hosts for magnetic dopants, materials that maximize the geometric factors in Eqs. 5-6 will provide large MCAEs in tetragonal and orthorhombic phases. For tetragonal ferroelectrics, a large c/a ratio is desirable. In this context, several bulk "super-tetragonal" ferroelectric phases with large c/a ratios may be of particular interest, such as $BiFeO_3$ [79] with c/a=1.23 and $BiCoO_3$ with c/a=1.27 [80]. Similar c/a ratios can be obtained in $PbTiO_3$ thin films through strain engineering [81]. For orthorhombic ferroelectrics, materials with the ratio $2a/\sqrt{b^2+c^2}$ as small as possible is desired. In addition, choosing A and/or B cations with sizeable spin-orbit coupling will further increase the MCAE. Theoretical approaches that compute the admixture of the spin-orbit coupling from the A-site orbitals with that of the magnetic ion [82] can aid in optimizing the choice of A-site cation.

In summary, we have determined the influence of the local crystalline environment on the MCAE of a Fe^{3+} dopant in the ferroelectric $BaTiO_3$. The polar displacement of Fe^{3+} is substantially reduced compared to that of Ti^{4+}, allowing the application of a Superposition Model with a centered dopant position to predict MCAEs. We test the centered model on several other ferroelectric oxide hosts and magnetic dopants and show that it successfully captures experimental MCAE trends. The implication of this result is that the local crystalline environment provided by the host, rather than its spin-orbit coupling strength, is key for determining the MCAE. This insight can be utilized to construct high-throughput screening of databases such as the Materials Project for promising ferroelectric hosts and magnetic dopants. Estimations of sign and magnitude of the MCAE from such a screening could guide towards ferroelectric oxide hosts which facilitate dramatic changes of MCAE near phase-change boundaries.

V. ACKNOWLEDGMENTS

This research was supported by the National Science Foundation Division of Materials Research under grant no. DMR-2223486. This work used the Expanse cluster at the San Diego Supercomputer Center through allocation MAT230011 from the Advanced Cyberinfrastructure Coordination Ecosystem: Services & Support (ACCESS) program [83], which is supported by National Science Foundation grants 2138259, 2138286, 2138307, 2137603, and 2138296. Work at the Molecular Foundry was supported by the Office of Science, Office of Basic Energy Sciences, of the U.S. Department of Energy under Contract No. DE-AC02-05CH11231. KI acknowledges support from the EPSRC (EP/W028131/1).

Appendix A: Appendix A: Magnetic anisotropy constants

We fit the DFT-computed MCAE surfaces from Fig. 2 to sums of products of trigonometric functions, appropriate for the particular crystalline symmetry[84]. The coefficients are the magnetic anisotropy constants K (distinct from the constants $b_2^0 = D$, $1/3b_2^2 = E$, $2/5b_4^4 = a$, from the spin Hamiltonian). The MCAE fitting function for the T phase is

$$\begin{aligned} U_{\mathrm{aniso}} =& K_1 \sin^2\theta + K_2 \sin^4\theta + K_{2'} \sin^4\theta \cos(4\phi) \\ &+ K_3 \sin^6\theta + K_{3'} \sin^6\theta \cos(4\phi)\,, \end{aligned} \tag{A1}$$

with magnetic anisotropy constants $K_1 = -78.0$, $K_2 = -6.4$, $K_{2'} = 1.1$, $K_3 = 3.2$, $K_{3'} = -1.1$ (all μeV), all obtained by fitting the DFT-computed MCAE presented in the main text.

For the O phase, Ref. [85] arrives at a form of a fitting function from squares of standard Cartesian direction cosines. We instead derive a fitting function based on the expansion of the MCAE with a basis set of spherical harmonics, and

then expand the elementary trigonometric functions. This gives, to sixth order in $\sin\theta$, the fitting function

$$\begin{aligned} U_{\text{aniso}} =& K_1 \sin^2\theta + K_{1'} \sin^2\theta \cos(2\phi) + K_2 \sin^4\theta \\ &+ K_{2'} \sin^4\theta \cos(2\phi) + K_{2''} \sin^4\theta \cos(4\phi) \\ &+ K_3 \sin^6\theta + K_{3'} \sin^6\theta \cos(2\phi) \\ &+ K_{3''} \sin^6\theta \cos(4\phi) + K_{3'''} \sin^6\theta \cos(6\phi)\,. \end{aligned} \tag{A2}$$

The values of these anisotropy constants are $K_1 = 41.2$, $K_{1'} = -0.8$, $K_2 = -12.7$, $K_{2'} = 10.2$, $K_{2''} = 0.4$, $K_3 = 7.6$, $K_{3'} = -7.7$, $K_{3''} = -0.2$, and $K_{3'''} = 0.2$ (all μeV).

This function for the magnetic anisotropy energy is in fact equivalent (to fourth order in $\sin\theta$) to that from Ref. [86],

$$\begin{aligned} U_{\text{aniso}} =& \sin^2\theta (K_1' \cos^2\phi + K_2' \sin^2\phi) \\ &+ \sin^4\theta (K_3' \cos^4\phi + K_4' \sin^2\phi \cos^2\phi + K_5' \sin^4\phi) \\ &+ \sin^2\theta \cos^2\theta (K_6' \cos^2\phi + K_7' \sin^2\phi)\,, \end{aligned} \tag{A3}$$

using K' to denote the convention for anisotropy constants in that work. However, the convention in the present work explicitly indicates only five independent anisotropy constants through fourth order in $\sin\theta$, and the method easily generalizes to any point group[87].

The small magnitude for the rhombohedral $R3m$ phase is nearly the convergence criterion for total energies (0.1 μeV), so the surface in Fig. 2(c) is fit to a function that is second order in $\sin\theta$, appropriate for rhombohedral systems[88, 89]

$$\text{MCAE}(\theta,\phi) = \sin^2(\theta-\theta_0)[K + K' \cos(2(\phi-\phi_0))]\,. \tag{A4}$$

The values of the fitting parameters are $K = -6.1$ μeV, $K' = 2.1$ μeV, $\theta_0 = -0.52°$, $\phi_0 = -1.13°$.

The surface with as-computed values is presented in the SI[48].)

Appendix B: Appendix B: Centered model calculation of b_2^0 with DFT lattice parameters

Table A1 shows centered model calculations of b_2^0 from Eqs. 5-7, performed using DFT-relaxed lattice parameters. Both PBEsol and LDA functionals are considered. Trends in b_2^0 values from Table III are reproduced.

TABLE A1. Estimates of b_2^0 from the centered model for specified magnetic dopants in specified hosts. We use the same $\bar{b}_2(R_0)$ and t_2 parameters as in Table III of the main text: for Fe^{3+} dopants we use $\bar{b}_2(R_0) = -0.437$ cm^{-1} and t_2=8, and for Mn^{2+} dopants we use $\bar{b}_2(R_0) = -0.1575$ cm^{-1} and t_2=7. Lattice parameters are given in Å and b_2^0 values are given in units of 10^{-4} cm^{-1}.

Ion	Host	Geometry (PBE)	b_2^0 (PBE)	Geometry (LDA)	b_2^0 (LDA)
Fe^{3+}	$BaTiO_3(T)$	a=3.970, c= 4.049	2008	a=3.943, c=3.992	1382
Fe^{3+}	$BaTiO_3(O)$	a=3.963, b=5.683, c= 5.705	-1662	a=3.939, b=5.613, c=5.623	-953
Fe^{3+}	$BaTiO_3(R)$	a=4.006, α= 89.86°	-94	a=3.962, α= 89.93°	-50
Fe^{3+}	$KNbO_3(T)$	a=3.970, c= 4.057	2210	a=3.945, c=3.990	1269
Fe^{3+}	$KNbO_3(O)$	a=3.962, b=5.679, c= 5.695	-1554	a=3.941, b=5.613, c=5.62	-879
Fe^{3+}	$KNbO_3(R)$	a=4.002, α= 89.91°	-64	a=3.962, α= 89.96°	-32
Mn^{2+}	$BaTiO_3(T)$	a=3.970, c= 4.049	604	a=3.943, c=3.992	411
Mn^{2+}	$BaTiO_3(O)$	a=3.963, b=5.683, c= 5.705	-498	a=3.939, b=5.613, c=5.623	-283
Mn^{2+}	$BaTiO_3(R)$	a=4.006, α= 89.86°	-32	a=3.962, α= 89.93°	-16
Fe^{3+}	$PBTiO_3(T)$	a=3.878, c= 4.186	7587	a=3.865, c=4.033	4935

[1] J. Liu, J. Mrozek, W. K. Myers, G. A. Timco, R. E. P. Winpenny, B. Kintzel, W. Plass, and A. Ardavan, Electric Field Control of Spins in Molecular Magnets, Phys. Rev. Lett. **122**, 037202 (2019).

[2] R. Hanson and D. D. Awschalom, Coherent manipulation of single spins in semiconductors, Nature **453**, 1043 (2008).

[3] J. van Slageren, Spin–electric coupling, Nat. Mater. **18**, 300 (2019).
[4] A. Chiesa, P. Santini, E. Garlatti, F. Luis, and S. Carretta, Molecular nanomagnets: a viable path toward quantum information processing?, Reports on Progress in Physics **87**, 034501 (2024).
[5] C. M. Leung, J. Li, D. Viehland, and X. Zhuang, A review on applications of magnetoelectric composites: From heterostructural uncooled magnetic sensors, energy harvesters to highly efficient power converters, J. Phys. D **51**, 263002 (2018).
[6] Y. Cheng, B. Peng, Z. Hu, Z. Zhou, and M. Liu, Recent development and status of magnetoelectric materials and devices, Phys. Lett. A **382**, 3018 (2018).
[7] M. Fittipaldi, A. Cini, G. Annino, A. Vindigni, A. Caneschi, and R. Sessoli, Electric field modulation of magnetic exchange in molecular helices, Nat. Mater. **18**, 329 (2019).
[8] P. Kot, M. Ismail, R. Drost, J. Siebrecht, H. Huang, and C. R. Ast, Electric control of spin transitions at the atomic scale, Nature Communications **14**, 6612 (2023).
[9] M. Fiebig, Revival of the magnetoelectric effect, J. Phys. D **38**, R123 (2005).
[10] R. Ramesh and N. A. Spaldin, Multiferroics: progress and prospects in thin films, Nat. Mater. **6**, 21 (2007).
[11] N. A. Spaldin and R. Ramesh, Advances in magnetoelectric multiferroics, Nat. Mater. **18**, 203 (2019).
[12] J. Liu, J. Mrozek, W. K. Myers, G. A. Timco, R. E. P. Winpenny, B. Kintzel, W. Plass, and A. Ardavan, Electric Field Control of Spins in Molecular Magnets, Phys. Rev. Lett. **122**, 037202 (2019).
[13] F. Wang, W. Shen, Y. Shui, J. Chen, H. Wang, R. Wang, Y. Qin, X. Wang, J. Wan, M. Zhang, *et al.*, Electrically controlled nonvolatile switching of single-atom magnetism in a Dy@ C84 single-molecule transistor, Nature Communications **15**, 2450 (2024).
[14] J. Nossa, M. Islam, M. R. Pederson, and C. M. Canali, Electric control of spin states in frustrated triangular molecular magnets, Physical Review B **107**, 245402 (2023).
[15] M. Islam, K. P. Withanage, C. Canali, and M. R. Pederson, Noncollinear first-principles studies of the spin-electric coupling in frustrated triangular molecular magnets, Physical Review B **109**, 214407 (2024).
[16] S. Bayliss, D. Laorenza, P. Mintun, B. Kovos, D. E. Freedman, and D. Awschalom, Optically addressable molecular spins for quantum information processing, Science **370**, 1309 (2020).
[17] J. Liu, V. V. Laguta, K. Inzani, W. Huang, S. Das, R. Chatterjee, E. Sheridan, S. M. Griffin, A. Ardavan, and R. Ramesh, Coherent electric field manipulation of Fe^{3+} spins in $PbTiO_3$, Sci. Adv. **7**, eabf8103 (2021).
[18] K. Inzani, N. Pokhrel, N. Leclerc, Z. Clemens, S. P. Ramkumar, S. M. Griffin, and E. A. Nowadnick, Manipulation of spin orientation via ferroelectric switching in Fe-doped Bi_2WO_6 from first principles, Phys. Rev. B **105**, 054434 (2022).
[19] A. W. Hewat, Structure of rhombohedral ferroelectric barium titanate, Ferroelectrics **6**, 215 (1973).
[20] H. Landolt, R. Boörnstein, K. Hellwege, D. Bimberg, M. Schulz, H. Weiss, and O. Madelung, *Landolt-Boörnstein Numerical Data and Functional Relationships in Science and Technology. Group 3: Crystal and Solid State Physics*, Vol. 17 Semiconductors (New series) (Springer, 1982).
[21] I. Bersuker, On the origin of ferroelectricity in perovskite-type crystals, Phys. Lett. **20**, 589 (1966).
[22] N. A. Pertsev, A. G. Zembilgotov, and A. K. Tagantsev, Effect of Mechanical Boundary Conditions on Phase Diagrams of Epitaxial Ferroelectric Thin Films, Phys. Rev. Lett. **80**, 1988 (1998).
[23] A. Hornig, R. Rempel, and H. Weaver, Electron paramagnetic resonance in single crystals of $BaTiO_3$, J. Phys. Chem. Solids **10**, 1 (1959).
[24] T. Sakudo, Electron Spin Resonance of Fe^{3+} in $BaTiO_3$ at Low Temperatures, J. Phys. Soc. Jpn **18**, 1626 (1963).
[25] T. Sakudo and H. Unoki, Electron Spin Resonance of Fe^{3+} in $BaTiO_3$ in the Rhombohedral and the Cubic Phases., J. Phys. Soc. Jpn **19**, 2109 (1964).
[26] D. Newman and E. Siegel, Superposition model analysis of Fe^{3+} and Mn^{2+} spin-Hamiltonian parameters, J. Phys. C **9**, 4285 (1976).
[27] D. Newman and W. Urban, Interpretation of S-state ion E.P.R. spectra, Adv. Phys. **24**, 793 (1975).
[28] E. Siegel and K. A. Müller, Local position of Fe^{3+} in ferroelectric $BaTiO_3$, Phys. Rev. B **20**, 3587 (1979).
[29] T. Takeda, Electron Spin Resonance of Gd^{3+} in Orthorhombic and Rhombohedral Phases of $BaTiO_3$, J. Phys. Soc. Jpn **24**, 533 (1968).
[30] J. P. Perdew, A. Ruzsinszky, G. I. Csonka, O. A. Vydrov, G. E. Scuseria, L. A. Constantin, X. Zhou, and K. Burke, Restoring the Density-Gradient Expansion for Exchange in Solids and Surfaces, Phys. Rev. Lett. **100**, 136406 (2008).
[31] G. Kresse and J. Hafner, Ab initio molecular dynamics for liquid metals, Phys. Rev. B **47**, 558 (1993).
[32] G. Kresse and J. Furthmüller, Efficiency of ab-initio total energy calculations for metals and semiconductors using a plane-wave basis set, Comput. Mater. Sci. **6**, 15 (1996).
[33] G. Kresse and J. Furthmüller, Efficient iterative schemes for ab initio total-energy calculations using a plane-wave basis set, Phys. Rev. B **54**, 11169 (1996).
[34] G. Kresse and D. Joubert, From ultrasoft pseudopotentials to the projector augmented-wave method, Phys. Rev. B **59**, 1758 (1999).
[35] P. E. Blöchl, Projector augmented-wave method, Phys. Rev. B **50**, 17953 (1994).
[36] S. L. Dudarev, G. A. Botton, S. Y. Savrasov, C. J. Humphreys, and A. P. Sutton, Electron-energy-loss spectra and the structural stability of nickel oxide: An LSDA+U study, Phys. Rev. B **57**, 1505 (1998).
[37] G. C. Moore, M. K. Horton, E. Linscott, A. M. Ganose, M. Siron, D. D. O'Regan, and K. A. Persson, High-throughput determination of Hubbard U and Hund J values for transition metal oxides via the linear response formalism, Phys. Rev. Mater. **8**, 014409 (2024).

[38] E. S. Kirkpatrick, K. A. Müller, and R. S. Rubins, Strong Axial Electron Paramagnetic Resonance Spectrum of Fe^{3+} in $SrTiO_3$ Due to Nearest-Neighbor Charge Compensation, Phys. Rev. **135**, A86 (1964).

[39] G. Shirane, H. Danner, and R. Pepinsky, Neutron Diffraction Study of Orthorhombic $BaTiO_3$, Phys. Rev. **105**, 856 (1957).

[40] W. Schildkamp and K. Fischer, Rhomboedric $BaTiO_3$. Structure studies at 132 K and 196 K, Z. Kristallogr. Cryst. Mater. **155**, 217 (1981).

[41] V. Lebedev, Quadratures on a sphere, USSR Computational Mathematics and Mathematical Physics **16**, 10 (1976).

[42] T. Camminady, SphericalQuadPy, `https://github.com/thomascamminady/sphericalquadpy/tree/master/sphericalquadpy` (2019).

[43] S. P. Ong, W. D. Richards, A. Jain, G. Hautier, M. Kocher, S. Cholia, D. Gunter, V. L. Chevrier, K. A. Persson, and G. Ceder, Python Materials Genomics (pymatgen): A robust, open-source python library for materials analysis, Comput. Mater. Sci. **68**, 314 (2013).

[44] A. Togo and I. Tanaka, {Spglib}: a software library for crystal symmetry search, arXiv preprint arXiv:1808.01590 (2018).

[45] H. T. Stokes and D. M. Hatch, FINDSYM: program for identifying the space-group symmetry of a crystal, J. Appl. Crystallogr. **38**, 237 (2005).

[46] K. Momma and F. Izumi, VESTA: a three-dimensional visualization system for electronic and structural analysis, J. Appl. Crystallogr. **41**, 653 (2008).

[47] D. A. Varshalovich, A. N. Moskalev, and V. K. Khersonskii, WIGNER D-FUNCTIONS, in *Quantum Theory of Angular Momentum* (WORLD SCIENTIFIC, 1988) Chap. Chapter 4, pp. 72–129.

[48] See Supplemental Material at [URL will be inserted by publisher] for details of atomic geometries and matrix elements of the Spin Hamiltonian.

[49] R. D. Shannon, Revised effective ionic radii and systematic studies of interatomic distances in halides and chalcogenides, Acta Crystallogr. Section A **32**, 751 (1976).

[50] D. J. Newman, Superposition model analysis of spin Hamiltonian parameters, J. Phys. C **15**, 6627 (1982).

[51] P. Bruno, Tight-binding approach to the orbital magnetic moment and magnetocrystalline anisotropy of transition-metal monolayers, Phys. Rev. B **39**, 865 (1989).

[52] D.-s. Wang, R. Wu, and A. J. Freeman, First-principles theory of surface magnetocrystalline anisotropy and the diatomic-pair model, Phys. Rev. B **47**, 14932 (1993).

[53] H. Wieder, Electrical behavior of barium titanatge single crystals at low temperatures, Physical Review **99**, 1161 (1955).

[54] M. W. Haverkort, Spin and orbital degrees of freedom in transition metal oxides and oxide thin films studied by soft x-ray absorption spectroscopy (2005), arXiv:cond-mat/0505214 [cond-mat.str-el].

[55] C. Rudowicz and P. Budzyński, Electron magnetic resonance studies of Fe^{3+} ions in $BaTiO_3$: Implications of the misinterpretation of zero-field splitting terms and comparative data analysis, Phys. Rev. B **74**, 054415 (2006).

[56] M. Actis and F. Michel-Calendini, Impurity levels and nonlinear optical properties of doped $BaTiO_3$ from extended cluster LDA calculations, Int. J. Quantum Chem. **61**, 657 (1997).

[57] D. L. Decker, K. Huang, and H. M. Nelson, Electron paramagnetic resonance measurements near the tricritical point in $BaTiO_3$, Phys. Rev. B **66**, 174103 (2002).

[58] M. B. Klein and R. Schwartz, Photorefractive effect in $BaTiO_3$: microscopic origins, JOSA B **3**, 293 (1986).

[59] L. Rimai and G. A. deMars, Electron Paramagnetic Resonance of Trivalent Gadolinium Ions in Strontium and Barium Titanates, Phys. Rev. **127**, 702 (1962).

[60] Y. Babu, M. Sastry, B. A. Dasannacharya, S. Balakumar, R. Ilangovan, P. Ramasamy, and M. Aggarwal, The tetragonal phase transition in mixed perovskite Ba1-xCaxTiO3 single crystals: EPR evidence of impurity-induced dynamic effects, J. Phys. Condens. Matter **8**, 7847 (1996).

[61] M. Sastry, M. Moghbel, P. Venkateswarlu, and A. Darwish, Experimental evidence of photoinduced valence change of Fe^{3+} in $BaTiO_3$ and mechanism for growth of new grating in depleted pump condition: An EPR investigation, Pramana **56**, 667 (2001).

[62] E. Possenriede, P. Jacobs, and O. Schirmer, Paramagnetic defects in $BaTiO_3$ and their role in light-induced charge transport. I. ESR studies, J. Phys. Condens. Matter **4**, 4719 (1992).

[63] H. Takayama, K.-P. Bohnen, and P. Fulde, Magnetic surface anisotropy of transition metals, Phys. Rev. B **14**, 2287 (1976).

[64] H. Watanabe, On the Ground Level Splitting of Mn++ and Fe+++ in Nearly Cubic Crystalline Field, Prog. Theor. Phys **18**, 405 (1957).

[65] M. Blume and R. Orbach, Spin-Lattice Relaxation of S-State Ions: Mn^{2+} in a Cubic Environment, Phys. Rev. **127**, 1587 (1962).

[66] Y. Wan-Lun and Z. Min-Guang, Spin-Hamiltonian parameters of ^{6}state ions, Phys. Rev. B **37**, 9254 (1988).

[67] D. J. Newman and B. Ng, *Crystal Field Handbook*, Vol. 43 (Cambridge University Press Cambridge, 2000).

[68] E. Siegel and K. A. Müller, Structure of transition-metal—oxygen-vacancy pair centers, Phys. Rev. B **19**, 109 (1979).

[69] G. Shirane, H. Danner, and R. Pepinsky, Neutron Diffraction Study of Orthorhombic $BaTiO_3$, Phys. Rev. **105**, 856 (1957).

[70] A. W. Hewat, Cubic-tetragonal-orthorhombic-rhombohedral ferroelectric transitions in perovskite potassium niobate: neutron powder profile refinement of the structures, J. Phys. C **6**, 2559 (1973).

[71] E. Siegel, W. Urban, K. Mueller, and E. Wiesendanger, Electron paramagnetic resonance of Fe^{3+} in $KNbO_3$ at 300 K, Phys. Lett. A **53**, 415 (1975).

[72] H. Ikushima, Electron Spin Resonance of Mn^{2+} in $BaTiO_3$ Single Crystal, J. Phys. Soc. Jpn **21**, 1866 (1966).

[73] F. Jona and G. G. Shirane, *Ferroelectric Crystals*, International series of monographs in solid state physics (Pergamon, 1962).

[74] G. Shirane, R. Pepinsky, and B. Frazer, X-ray and neutron diffraction study of ferroelectric $PbTiO_2$, Acta Crystallogr. **9**, 131 (1956).

[75] B. Jaffe, W. R. Cook, and H. Jaffe, *Piezoelectric Ceramics* (Elsevier, 1971) Chap. 2 - The piezoelectric effect in ceramics, pp. 7–21.

[76] T. Dunn, Spin-orbit coupling in the first and second transition series, Trans. Faraday Soc. **57**, 1441 (1961).

[77] I. G. Rau, S. Baumann, S. Rusponi, F. Donati, S. Stepanow, L. Gragnaniello, J. Dreiser, C. Piamonteze, F. Nolting, S. Gangopadhyay, O. R. Albertini, R. M. Macfarlane, C. P. Lutz, B. A. Jones, P. Gambardella, A. J. Heinrich, and H. Brune, Reaching the magnetic anisotropy limit of a 3¡i¿d¡/i¿ metal atom, Science **344**, 988 (2014).

[78] N. A. Spaldin, *Magnetic Materials: Fundamentals and Applications*, 2nd ed. (Cambridge University Press, 2010).

[79] H. Béa, B. Dupé, S. Fusil, R. Mattana, E. Jacquet, B. Warot-Fonrose, F. Wilhelm, A. Rogalev, S. Petit, V. Cros, A. Anane, F. Petroff, K. Bouzehouane, G. Geneste, B. Dkhil, S. Lisenkov, I. Ponomareva, L. Bellaiche, M. Bibes, and A. Barthélémy, Evidence for Room-Temperature Multiferroicity in a Compound with a Giant Axial Ratio, Phys. Rev. Lett. **102**, 217603 (2009).

[80] A. A. Belik, S. Iikubo, K. Kodama, N. Igawa, S.-i. Shamoto, S. Niitaka, M. Azuma, Y. Shimakawa, M. Takano, F. Izumi, *et al.*, Neutron powder diffraction study on the crystal and magnetic structures of $BiCoO_3$, Chem. Mater. **18**, 798 (2006).

[81] L. Zhang, J. Chen, L. Fan, O. Diéguez, J. Cao, Z. Pan, Y. Wang, J. Wang, M. Kim, S. Deng, *et al.*, Giant polarization in super-tetragonal thin films through interphase strain, Science **361**, 494 (2018).

[82] R. de Sousa, M. Allen, and M. Cazayous, Theory of Spin-Orbit Enhanced Electric-Field Control of Magnetism in Multiferroic $BiFeO_3$, Phys. Rev. Lett. **110**, 267202 (2013).

[83] T. J. Boerner, S. Deems, T. R. Furlani, S. L. Knuth, and J. Towns, Access: Advancing innovation: NSF's advanced cyberinfrastructure coordination ecosystem: Services & support, in *Practice and Experience in Advanced Research Computing* (Association for Computing Machinery, New York, NY, USA, 2023) pp. 173–176.

[84] L. Landau and E. Lifshitz, CHAPTER V - FERROMAGNETISM AND ANTIFERROMAGNETISM, in *Electrodynamics of Continuous Media (Second Edition)*, Course of Theoretical Physics, Vol. 8, edited by L. Landau and E. Lifshitz (Pergamon, Amsterdam, 1984) second edition ed., pp. 130–179.

[85] O. Zhdanova, M. Lyakhova, and Y. G. Pastushenkov, Magnetic properties and domain structure of FeB single crystals, Metal Science and Heat Treatment **55**, 68 (2013).

[86] W. P. Mason, Derivation of Magnetostriction and Anisotropic Energies for Hexagonal, Tetragonal, and Orthorhombic Crystals, Phys. Rev. **96**, 302 (1954).

[87] B. A. Barker, S. M. Griffin, and E. A. Nowadnick, Derivation of magnetic anisotropy energy formulae for all point group symmetries.

[88] A. Schrön, C. Rödl, and F. Bechstedt, Crystalline and magnetic anisotropy of the $3d$-transition metal monoxides MnO, FeO, CoO, and NiO, Phys. Rev. B **86**, 115134 (2012).

[89] R. Skomski, *Simple Models of Magnetism* (Oxford University Press, 2008).